Journal of Sound and Vibration (2000) **237**(3), 435–455
doi:10.1006/jsvi.2000.3067, available online at http://www.idealibrary.com on IDEAL®

NON-LINEAR DYNAMIC RESPONSE OF A SPUR GEAR PAIR: MODELLING AND EXPERIMENTAL COMPARISONS

R. G. PARKER

Department of Mechanical Engineering, Ohio State University, Columbus, OH 43210-1107, *USA.*
E-mail: parker.242@osu.edu

S. M. VIJAYAKAR

Advanced Numerical Solutions, 3554 *Mark Twain Court, Hilliard, OH* 43026, *USA*

AND

T. IMAJO

Komatsu, Ltd. 3-1-1, *Ueno, Hirakata-City, Osaka*, 573-1011, *Japan*

(*Received* 10 *November* 1999, *and in final form* 20 *April* 2000)

The dynamic response of a spur gear pair is investigated using a finite element/contact mechanics model that offers significant advantages for dynamic gear analyses. The gear pair is analyzed across a wide range of operating speeds and torques. Comparisons are made to other researchers' published experiments that reveal complex non-linear phenomena. The non-linearity source is contact loss of the meshing teeth, which, in contrast to the prevailing understanding, occurs even for large torques despite the use of high-precision gears. A primary feature of the modelling is that dynamic mesh forces are calculated using a detailed contact analysis at each time step as the gears roll through the mesh; there is no need to externally specify the excitation in the form of time-varying mesh stiffness, static transmission error input, or the like. A semi-analytical model near the tooth surface is matched to a finite element solution away from the tooth surface, and the computational efficiency that results permits dynamic analysis. Two-single-degree-of-freedom models are also studied. While one gives encouragingly good results, the other, which appears to have better mesh stiffness modelling, gives poor comparisons with experiments. The results indicate the sensitivity of such models to the Fourier spectrum of the changing mesh stiffness.

1. INTRODUCTION

The dynamic response of gears remains a paramount concern because of noise generation and dynamic loads. Prior studies have yielded a vast literature on this topic and, in particular, a remarkable variety of mathematical models as discussed in reference [1]. More recent studies are cited in the comprehensive bibliography in reference [2]. Most models use a discrete (lumped parameter) representation involving rigid gear components and combinations of discrete elastic and dissipative elements to represent the meshing teeth and support/bearing stiffnesses. Such models have varying complexity in their treatment of the tooth mesh, shaft, bearing, and housing modelling. In essence, the required analytical modelling to capture the complex gear dynamic response has not been established. Even when attention is restricted to modelling the tooth mesh, a variety of plausible

0022-460X/00/430435 + 21 $35.00/0

representations exist [3], and the optimal treatment of time-varying mesh stiffness, contact loss, use of static transmission error as a dynamic input, frictional effects, etc., remains unsettled. This study analytically investigates the dynamics of a spur gear pair for which comprehensive experimental data exist. The tooth mesh is the most complex aspect in gear dynamics, and the gear system in this work is selected to isolate tooth mesh effects. The primary analytical tool is a finite elements/contact mechanics (FE/CM) formulation that offers significant advantages in its representation of the crucial tooth contact. The purpose is to further expose the basic non-linear and time-varying phenomena at play in the tooth mesh, demonstrate the modelling fidelity and advantages of the FE/CM method used, and compare the ability of two s.d.o.f models to represent the experimentally observed phenomena.

The gear pair studied is that used in a series of experiments by Kahraman and Blankenship [4–8]. Tests on this system were initially reported in reference [8], where the details of the system are given. The test stand is designed to isolate the impact of tooth mesh interactions on the dynamic response and exclude complications from the shafts, bearings, and housing. In particular, the bearing and shaft configuration is such that the support structure is nearly rigid and the response is purely gear rotation. The test gears are dynamically isolated from the slave gears in the back-to-back configuration. Despite this reduction to the simplest case of s.d.o.f response, measurements of dynamic transmission error (DTE) show distinct, repeatable, non-linear, time-varying system response in the form of classical jump phenomena, sub- and super-harmonic resonances, parametric instabilities, and even apparently chaotic response. The non-linear tooth mesh forces causing these complex behaviors are what we seek to model in this study.

A primary motivation is to establish the ability of the unique FE/CM formulation to capture complex gear mesh forces in dynamics simulations. Similar analysis tools with the advantages presented in what follows are not known to the authors. Conventional finite element analysis, and even the currently available commercial software, require prohibitively refined meshes to represent the tooth contact and precise tooth surface description needed for gear mechanics, particularly when one seeks to go beyond static analyses to *dynamic* response analyses. The subject gear system was selected to validate the FE/CM approach as a research tool because (1) the complex, non-linear behavior is a suitably demanding benchmark, and (2) carefully conducted, high-quality experiments exist.

Traditional finite elements are effective for calculating quantities like mesh stiffness, tooth deflections, and stress distributions under *static* conditions where highly refined meshes are computationally feasible and the contact mechanics are simpler. Use of finite elements in *dynamic* gear analyses is typically restricted to components away from the tooth mesh such as the gear web, shafts and housing. Tooth mesh excitations are then *specified externally* and the response is calculated by conventional means. The current finite element formulation, however, is unique in representing the time-varying tooth contact mechanics with sufficient fidelity and computational efficiency so that dynamic analyses are possible. The two gears are numerically rolled through the mesh at a specified operating speed. Thus, the instantaneous configuration changes continuously as teeth enter and exit the mesh. This is why a full gear mesh is required (Figure 1) rather than a gear with one or two representative teeth. Contact analysis at each time step identifies the dynamic mesh forces due to changing numbers of teeth in mesh and contact loss, *eliminating the need for external specification of the dynamic forces or assumptions about modelling these mesh forces by time-varying stiffness and static transmission error*. The finite element results give remarkable agreement with the measured behavior. Furthermore, they clearly identify contact loss as the root cause of the non-linear response. An outline of this modelling and its features,

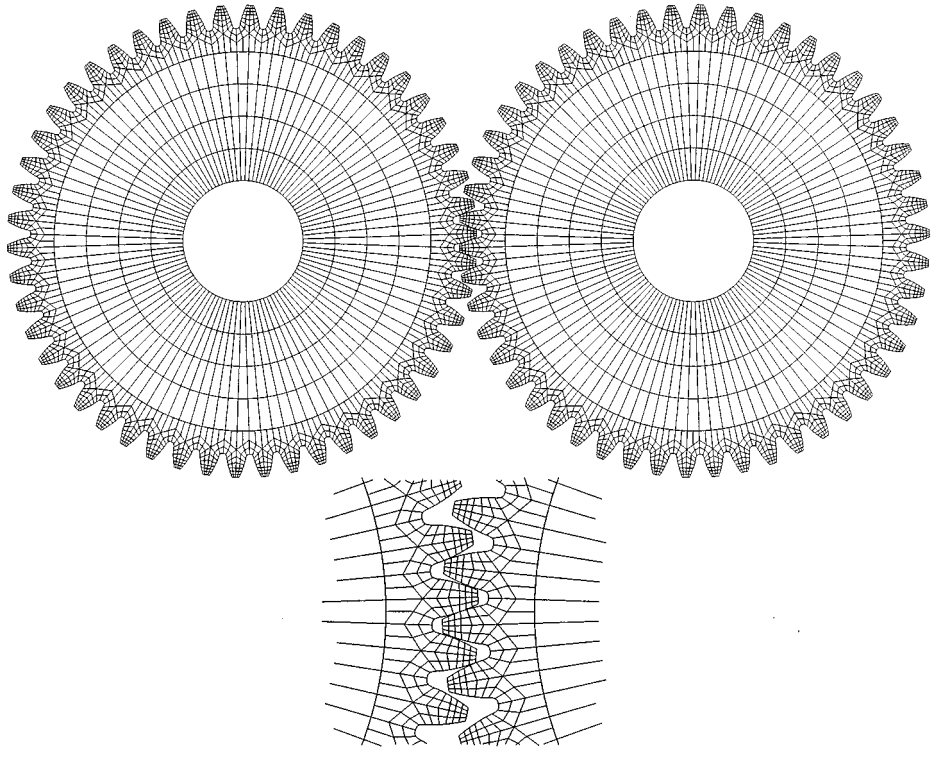

Figure 1. Finite element mesh and a close-up view of the mesh density on the teeth.

which has been used successfully for planetary gears [9], is presented subsequently. To examine simpler representations, results from two-s.d.o.f (SDOF) analytical models based on Figure 2 are given. While one of these gives encouragingly good results, neither of them are as accurate as the finite element model. Also, the one that might be expected to be the more accurate, fails to capture the critical behaviors.

2. FINITE ELEMENT ANALYSIS

The finite element formulation is unique in its combination of detailed contact modelling between the elastic teeth [10] with a combined surface integral/finite element solution [11] to efficiently capture tooth deformations and loads with a relatively coarse mesh. Details are available in the references and a short description of the surface integral/finite element solution is given in reference [9]. The contact analysis is briefly described here.

The mesh for the gear pair in this study is shown in Figure 1. Each of the gears undergoes large rotation according to a prescribed, kinematic trajectory. In this two-gear case, this trajectory is that of conjugate action of the gears at specified operating speed. The elastic gear motions that superpose on this prescribed trajectory are small. If the finite element displacement vector $\mathbf{x}_{fi}$ for a particular gear i is measured with respect to a reference frame that follows this known trajectory, then it is possible to represent its behavior by a linear system of equations

$$\mathbf{M}_{ffi}\ddot{\mathbf{x}}_{fi} + \mathbf{C}_{ffi}\dot{\mathbf{x}}_{fi} + \mathbf{K}_{ffi}\mathbf{x}_{fi} = \mathbf{f}_{fi}. \tag{1}$$

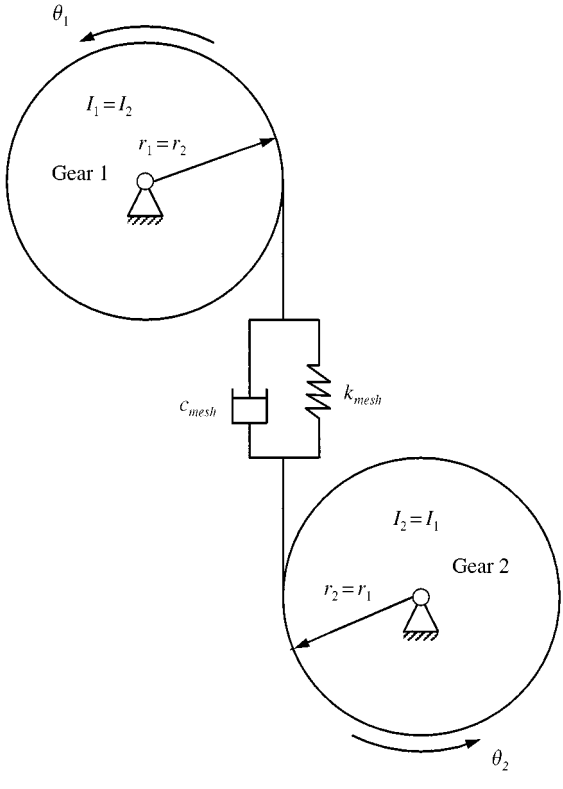

Figure 2. Single-degree-of-freedom modelling of the two gear system. The response is presented as the dynamic transmission error (DTE) $r_1\theta_1 + r_2\theta_2$.

Here, $\mathbf{f}_{fi}$ is a vector of specified external loads. The damping matrix $\mathbf{C}_{ffi}$ is obtained using Rayleigh's damping model

$$\mathbf{C}_{ffi} = \mu\mathbf{M}_{ffi} + \eta\mathbf{K}_{ffi}. \tag{2}$$

If the finite element mesh is adequately constrained to its reference frame, then $\mathbf{x}_{fi}$ contains no rigid-body degrees of freedom and $\mathbf{K}_{ffi}$ is positive-definite. $\mathbf{M}_{ffi}$ is always positive-definite.

Rigid-body d.o.f. are not assigned to the finite element mesh but rather to the moving reference frame. A vector $\mathbf{x}_{ri}$ represents the small "rigid-body" motions of the reference frame that superpose on the large, prescribed kinematic trajectory of the reference frame. For a general two-dimensional model, there are up to three unconstrained components in $\mathbf{x}_{ri}$. For the current system where translations of the gear centers are prevented, each gear has only one reference frame d.o.f. θ_i. Augmenting equation (1) with the vector $\mathbf{x}_{ri}$ and assuming that $\mathbf{x}_{ri}$ is small, we obtain the linear relationship

$$\begin{bmatrix} \mathbf{M}_{ffi} & \mathbf{M}_{fri} \\ \mathbf{M}_{rfi} & \mathbf{M}_{rri} \end{bmatrix} \begin{Bmatrix} \ddot{\mathbf{x}}_{fi} \\ \ddot{\mathbf{x}}_{ri} \end{Bmatrix} + \begin{bmatrix} \mathbf{C}_{ffi} & \mathbf{C}_{fri} \\ \mathbf{C}_{rfi} & \mathbf{C}_{rri} \end{bmatrix} \begin{Bmatrix} \dot{\mathbf{x}}_{fi} \\ \dot{\mathbf{x}}_{ri} \end{Bmatrix} + \begin{bmatrix} \mathbf{K}_{ffi} & \mathbf{K}_{fri} \\ \mathbf{K}_{rfi} & \mathbf{K}_{rri} \end{bmatrix} \begin{Bmatrix} \mathbf{x}_{fi} \\ \mathbf{x}_{ri} \end{Bmatrix} = \begin{Bmatrix} \mathbf{f}_{fi} \\ \mathbf{f}_{ri} \end{Bmatrix}. \tag{3}$$

The terms $\mathbf{M}_{rfi} = \mathbf{M}_{fri}^{\mathrm{T}}$ and $\mathbf{K}_{rfi} = \mathbf{K}_{fri}^{\mathrm{T}}$ are computed from the finite element mesh using energy methods. Any lumped masses and inertias are added into $\mathbf{M}_{rri}$. In a general system

where, for example, the gears are on elastic rather than rigid bearings, the bearings are modelled as lumped spring-damper elements connecting the individual gear reference frames to ground. These and any other lumped stiffnesses and viscous dampers contribute the terms $\mathbf{K}_{rri}$ and $\mathbf{C}_{rri}$ in equation (3). The equations for each gear are assembled into a larger system of equations for the entire system as

$$\begin{bmatrix} \mathbf{M}_{ff} & \mathbf{M}_{fr} \\ \mathbf{M}_{rf} & \mathbf{M}_{rr} \end{bmatrix} \begin{Bmatrix} \ddot{\mathbf{x}}_f \\ \ddot{\mathbf{x}}_r \end{Bmatrix} + \begin{bmatrix} \mathbf{C}_{ff} & \mathbf{C}_{fr} \\ \mathbf{C}_{rf} & \mathbf{C}_{rr} \end{bmatrix} \begin{Bmatrix} \dot{\mathbf{x}}_f \\ \dot{\mathbf{x}}_r \end{Bmatrix} + \begin{bmatrix} \mathbf{K}_{ff} & \mathbf{K}_{fr} \\ \mathbf{K}_{rf} & \mathbf{K}_{rr} \end{bmatrix} \begin{Bmatrix} \mathbf{x}_f \\ \mathbf{x}_r \end{Bmatrix} = \begin{Bmatrix} \mathbf{f}_f \\ \mathbf{f}_r \end{Bmatrix}. \tag{4}$$

$$\mathbf{x}_f = \begin{Bmatrix} \mathbf{x}_{f1} \\ \mathbf{x}_{f2} \\ \cdots \\ \mathbf{x}_{fi} \\ \cdots \end{Bmatrix}, \quad \mathbf{x}_r = \begin{Bmatrix} \mathbf{x}_{r1} \\ \mathbf{x}_{r2} \\ \cdots \\ \mathbf{x}_{ri} \\ \cdots \end{Bmatrix}, \quad \mathbf{f}_f = \begin{Bmatrix} \mathbf{f}_{f1} \\ \mathbf{f}_{f2} \\ \cdots \\ \mathbf{f}_{fi} \\ \cdots \end{Bmatrix}, \quad \mathbf{f}_r = \begin{Bmatrix} \mathbf{f}_{r1} \\ \mathbf{f}_{r2} \\ \cdots \\ \mathbf{f}_{ri} \\ \cdots \end{Bmatrix} \tag{5}$$

$$\Rightarrow \mathbf{M}\ddot{\mathbf{x}} + \mathbf{C}\dot{\mathbf{x}} + \mathbf{K}\mathbf{x} = \mathbf{f}, \quad \mathbf{x} = \begin{Bmatrix} \mathbf{x}_f \\ \mathbf{x}_r \end{Bmatrix}, \quad \mathbf{f} = \begin{Bmatrix} \mathbf{f}_f \\ \mathbf{f}_r \end{Bmatrix}. \tag{6}$$

The matrix $\mathbf{K}_{rr}$ is usually not of full rank in gear applications, so the stiffness matrix $\mathbf{K}$ is typically not invertible. This is the current case due to the unrestrained rigid-body rotation admitted for each of the two gears.

In static and quasi-static analyses, the inertia and damping matrices are neglected and the system (6) reduces to

$$\mathbf{K}\mathbf{x} = \mathbf{f}. \tag{7}$$

In dynamic analyses, time-discretization based on the Newmark method is used. The discretized form of equation (6) is

$$\begin{aligned} [\mathbf{M} + \gamma \Delta t \mathbf{C} + \beta \Delta t^2 \mathbf{K}]\mathbf{x}_{n+1} = &- [-2\mathbf{M} + (1 - 2\gamma)\Delta t \mathbf{C} + (1/2 - 2\beta + \gamma)\Delta t^2 \mathbf{K}]\mathbf{x}_n \\ &- [\mathbf{M} - (1 - \gamma)\Delta t \mathbf{C} + (1/2 + \beta - \gamma)\Delta t^2 \mathbf{K}]\mathbf{x}_{n-1} \\ &+ \Delta t^2 [\beta \mathbf{f}_{n+1} + (1/2 - 2\beta + \gamma)\mathbf{f}_n + (1/2 + \beta - \gamma)\mathbf{f}_{n-1}], \end{aligned} \tag{8}$$

$$\mathbf{x}_n = \mathbf{x}(t_0 + n\Delta t), \quad \mathbf{f}_n = \mathbf{f}(t_0 + n\Delta t). \tag{9}$$

All schemes for which $\gamma = \frac{1}{2}$ and $\beta \geqslant \frac{1}{4}$ are unconditionally stable and show no artificial damping. Several commonly used integration schemes are special cases of this three-point scheme for certain combinations of γ and β. The values $\gamma = \frac{1}{2}$ and $\beta = \frac{1}{4}$ are used here. Equation (8) can be written in the form $\hat{\mathbf{K}}\hat{\mathbf{x}} = \hat{\mathbf{f}}$, where $\hat{\mathbf{K}} = \mathbf{M} + \gamma \Delta t \mathbf{C} + \beta \Delta t^2 \mathbf{K}$ is an effective stiffness matrix, $\hat{\mathbf{x}} = \mathbf{x}_{n+1}$, and $\hat{\mathbf{f}}$ is an effective load vector. This is identical in form to equation (7) and they are treated identically in the discussion below.

A linear co-ordinate transformation is used to diagonalize the system (7) and separate out the non-singular part according to

$$\mathbf{x} = [\mathbf{T}_\phi \ \ \mathbf{T}_\theta] \begin{Bmatrix} \mathbf{q}_\phi \\ \mathbf{q}_\theta \end{Bmatrix} = \mathbf{T} \begin{Bmatrix} \mathbf{q}_\phi \\ \mathbf{q}_\theta \end{Bmatrix}, \quad \mathbf{T}^{\mathrm{T}}\mathbf{f} = \begin{bmatrix} \mathbf{T}_\phi^{\mathrm{T}} \\ \mathbf{T}_\theta^{\mathrm{T}} \end{bmatrix} \mathbf{f} = \begin{Bmatrix} \mathbf{g}_\phi \\ \mathbf{g}_\theta \end{Bmatrix}, \tag{10}$$

$$\mathbf{T}^{\mathrm{T}}\mathbf{K}\mathbf{T} \begin{Bmatrix} \mathbf{q}_\phi \\ \mathbf{q}_\theta \end{Bmatrix} = \begin{bmatrix} \mathbf{K}_{\phi\phi} & \mathbf{0} \\ \mathbf{0} & \mathbf{0} \end{bmatrix} \begin{Bmatrix} \mathbf{q}_\phi \\ \mathbf{q}_\theta \end{Bmatrix} = \begin{Bmatrix} \mathbf{g}_\phi \\ \mathbf{g}_\theta \end{Bmatrix} \tag{11}$$

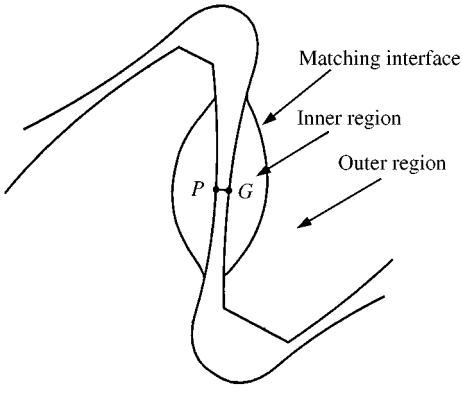

Figure 3. Contact zone indicating candidate contact points P and G. The inner and outer regions where the analytical (inner) and finite element (outer) solutions apply are shown.

where the columns of **T** contain the eigenvectors of **K**. The generalized co-ordinates are partitioned according to those associated with elastic modes ($\mathbf{q}_\phi$) and, if **K** is singular, with rigid-body modes ($\mathbf{q}_\theta$). $\mathbf{K}_{\phi\phi}$ is diagonal and positive-definite. For a dynamic situation, the effective stiffness matrix $\hat{\mathbf{K}}$ is always positive-definite, so that $\mathbf{q}_\theta$ would have a dimension of zero. The partitions of equation (11) give

$$\mathbf{q}_\phi = \mathbf{K}_{\phi\phi}^{-1}\,\mathbf{g}_\phi, \qquad \mathbf{g}_\theta = \mathbf{T}_\theta^{\mathrm{T}}\mathbf{f} = \mathbf{0}. \tag{12}$$

For the contact analysis, consider the pinion-gear combination shown in Figure 3. Candidate contact pairs (CCP) with surface normals along a common axis are calculated by a search algorithm with specified tolerance (P–G, for example). The tooth surface is defined with arbitrary precision as either a continuous curve or as a set of surface co-ordinates with a specified surface normal (these surface co-ordinates are *not* limited to nodal points on the finite element mesh). The (arbitrary) number of points used to describe the surface dictates the pool of possible contact points. The following vector quantities are defined: $\hat{\varepsilon}$ is the separation distances of all CCPs along their common normal at some instant in the unloaded and undeformed state, **d** is the separations of the CCPs along their common normal in the loaded, deformed state, δ = the changes in separation due to loading, and **p** is the compressive contact loads acting along the normals of each CCP. The final separation of the CCPs is given by

$$\mathbf{d} = \hat{\varepsilon} + \delta. \tag{13}$$

The external load vector **f** (from equation (7)) is related to the contact force vector **p** by the linear relationship

$$\mathbf{f} = \mathbf{E}\mathbf{p} + \mathbf{f}_o. \tag{14}$$

Here, **E** is a known, non-square matrix that apportions the contact force **p** at the CCPs as nodal forces at adjacent nodes. **E** depends on the geometry and finite element interpolation functions. $\mathbf{f}_o$ is a vector of applied, externally-specified, non-contact loads acting on the model. From equations (12) and (14),

$$\mathbf{q}_\phi = \mathbf{K}_{\phi\phi}^{-1}\mathbf{T}_\phi^{\mathrm{T}}(\mathbf{E}\mathbf{p} + \mathbf{f}_o) = (\mathbf{K}_{\phi\phi}^{-1}\mathbf{T}_\phi^{\mathrm{T}}\mathbf{E})\mathbf{p} + (\mathbf{K}_{\phi\phi}^{-1}\mathbf{T}_\phi^{\mathrm{T}})\mathbf{f}_o. \tag{15}$$

The increase in separation δ is related to the displacement vector of equation (6) according to

$$\delta = \mathbf{G}\mathbf{x} = \mathbf{G}\,[\mathbf{T}_\phi \;\; \mathbf{T}_\theta] \begin{Bmatrix} \mathbf{q}_\phi \\ \mathbf{q}_\theta \end{Bmatrix}. \tag{16}$$

Like $\mathbf{E}$ above, $\mathbf{G}$ depends on geometry and finite element interpolation functions. Equation (16) contains only the finite element contributions to the increase in separation at the contact points (from the outer-region model of Figure 3). In addition to this, a contribution from a local deformation field is superposed (from the inner-region model of Figure 3). This contribution is calculated using a semi-analytical surface integral/finite element solution near the contact zone [9, 11]. This introduces an additional term $\mathbf{A}_{local}\mathbf{p}$ into equation (16) to yield, in combination with equation (13) and (15), the compliance relationship

$$\begin{aligned} \mathbf{d} &= \hat{\varepsilon} + \delta = \hat{\varepsilon} + \mathbf{G}\mathbf{T}_\phi\mathbf{q}_\phi + \mathbf{G}\mathbf{T}_\theta\mathbf{q}_\theta + \mathbf{A}_{local}\mathbf{p} \\ &= (\mathbf{G}\mathbf{T}_\phi\mathbf{K}_{\phi\phi}^{-1}\mathbf{T}_\phi^{\mathrm{T}}\mathbf{E} + \mathbf{A}_{local})\mathbf{p} + \mathbf{G}\mathbf{T}_\theta\mathbf{q}_\theta + (\hat{\varepsilon} + \mathbf{G}\mathbf{T}_\phi\mathbf{K}_{\phi\phi}^{-1}\mathbf{T}_\phi^{\mathrm{T}}\mathbf{f}_o). \end{aligned} \tag{17}$$

This is cast in the final form

$$\begin{aligned} &\mathbf{d} = \mathbf{A}\mathbf{p} + \mathbf{C}\mathbf{q}_\theta + \varepsilon, \\ &\mathbf{A} = (\mathbf{G}\mathbf{T}_\phi\mathbf{K}_{\phi\phi}^{-1}\mathbf{T}_\phi^{\mathrm{T}}\mathbf{E} + \mathbf{A}_{local}), \qquad \mathbf{C} = \mathbf{G}\mathbf{T}_\theta, \qquad \varepsilon = \hat{\varepsilon} + \mathbf{G}\mathbf{T}_\phi\mathbf{K}_{\phi\phi}^{-1}\mathbf{T}_\phi^{\mathrm{T}}\mathbf{f}_o. \end{aligned} \tag{18}$$

In addition, the second of equation (12) and equation (14) lead to the equilibrium equation

$$\mathbf{T}_\theta^{\mathrm{T}}\mathbf{E}\mathbf{p} + \mathbf{T}_\theta^{\mathrm{T}}\mathbf{f}_o = \mathbf{0} \tag{19}$$

which is of the form

$$\mathbf{B}\mathbf{p} = \lambda, \qquad \mathbf{B} = \mathbf{T}_\theta^{\mathrm{T}}\mathbf{E}, \qquad \lambda = -\,\mathbf{T}_\theta^{\mathrm{T}}\mathbf{f}_o. \tag{20}$$

The contact problem is then posed as follows: solve equations (18) and (20) for $\mathbf{d}$, $\mathbf{p}$, and $\mathbf{q}_\theta$ subject to the constraints that all components d_i, $p_i \geqslant 0$ and either $d_i = 0$ or $p_i = 0$ holds for every i. This problem can be solved with linear programming methods [10]. The results are then used to determine the displacement $\mathbf{x}$ from equations (14), (10), and (12). The contact forces $\mathbf{p}$ can also be used in the combined surface integral/finite-element solution to calculate tooth deflections and stresses near the tooth contact zone. This process is repeated at each integration time step. $\mathbf{E}$ and $\mathbf{G}$, which depend on straightforward kinematics, are recalculated at each step as the gears undergo the specified rigid-body motions. $\mathbf{A}_{local}$ is also recalculated at each step because of the changing contact conditions. The finite element stiffness matrix $\mathbf{K}$ (or $\hat{\mathbf{K}}$ for dynamic analyses) and its eigenvectors $\mathbf{T} = [\mathbf{T}_\phi \;\; \mathbf{T}_\theta]$, however, are determined only once and do not require updating.

The combined surface integral/finite element solution is described in reference [11] with a simplified discussion in reference [9]. In essence, the concept is to match an analytical "inner" solution that applies near the tooth surface (calculated from the solution for a point load on a half-space) with an "outer" finite element solution that applies slightly away from the tooth surface where the displacement gradients are less steep. The need for an extremely refined tooth mesh is removed because the solution in the "inner" region at the tooth surface does *not* depend on finite elements to calculate the tooth surface deformations, model the contact mechanics, or define the geometry via node points (see the relatively coarse mesh in Figure 1(b)). This key point makes *dynamic* analysis with careful contact modelling possible for a sufficient number of time steps to obtain frequency domain response calculations.

A crucial distinction of this formulation is that no *a priori assumptions about the nature of the dynamic excitation are needed*. The time-varying mesh stiffness and/or static transmission error excitation that are required inputs in virtually all existing models (e.g., references [8, 12]) are naturally calculated outputs in this formulation. In addition, there is no agreement on how to incorporate one or both of these modelling devices into analytical representations, but this is not of concern in the computational model. Here, only the operating torque and speed, and not the dynamic excitation, are specified inputs to the dynamic analysis. The desired outputs are the rotational vibrations of each gear, expressed as the dynamic transmission error $DTE = r_1\theta_1 + r_2\theta_2$ (Figure 2), and the net tooth contact force calculated from the contact force vector $\mathbf{p}$ at each meshing tooth. Note that $\theta_{1,2}$ are the elements of $\mathbf{x}_r$ in equation (6).

The mesh in Figure 1 shows a tooth section mesh and a central gear mesh. A Fourier series expansion of the displacements on the circular joining interface is used to allow a mismatch of nodal positions between the two meshes. The somewhat crude central gear mesh is for computational efficiency as it is only necessary to capture inertial effects. Conventional four-node finite element displacement interpolation is used everywhere except at this interface between the central gear mesh and the tooth section mesh.

2.1. DYNAMIC TRANSMISSION ERROR

The experimental gear pair consists of identical, precision-ground spur gears with 50 teeth, 7·047 mm base radius, 3 mm module, and 20° pressure angle (Figure 1). This work considers only the case of no tooth modification and a fixed contact ratio of 1·75. While the actual facewidth is 20 mm, the two-dimensional finite element model uses unit facewidth of 1 in = 25·4 mm. The gears are steel with elasticity modulus of 207×10^9 N/m^2 and density of 7600 kg/m^3. To mimic the rigid support test set-up, the finite element and SDOF models constrain the gears to rotate about their centers with no translation.

Blankenship and Kahraman [4] state that the gears have a natural frequency "around" $f_n = 2700$ Hz. Numerical impact tests were conducted to calculate the natural frequency using finite element. The gears are held statically in mesh by a steady torque T_i. For a single integration time step, the torque is increased to 1·2 T_i, simulating an applied impulse. The natural frequency is determined from the ensuing transient DTE response. The natural frequencies for different torques and either one or two pairs of teeth in mesh are shown in Table 1. The mean (over one mesh cycle) finite element results are within 5% of the experimental value of $2700\sqrt{25{\cdot}4/20}$, where the scaling $\sqrt{25{\cdot}4/20}$ is dictated by the stiffness change associated with the differing facewidths in the experiment and computational model. Table 1 shows the natural frequency to be a weak function of load over this range of torques.

TABLE 1

Natural frequencies in Hz for differing torques and one/two pairs of meshing teeth

Toque	100 N m	200 N m	300 N m
One tooth pair in mesh	2480	2480	2560
Two tooth pairs in mesh	3040	3040	3040
Mean (over 1 mesh cycle)	2900	2900	2920

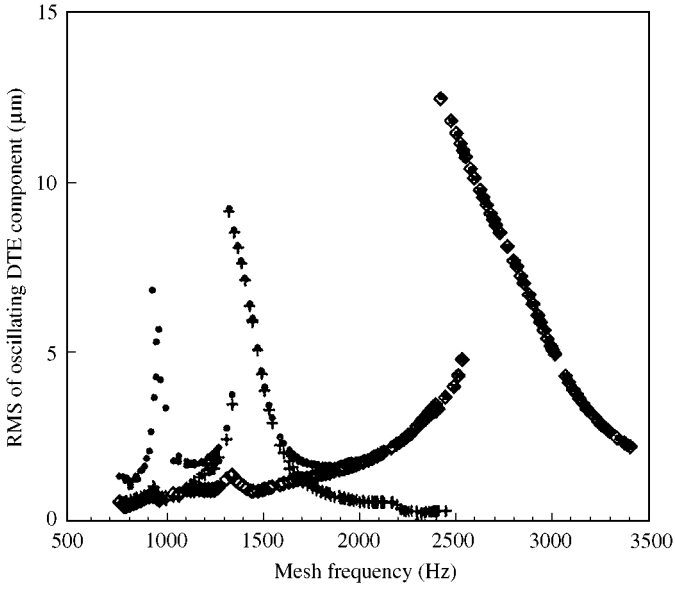

Figure 4. Experimentally measured RMS of oscillating component of dynamic transmission error for $T = 150$ N m. From reference [4].

A second purpose of these impact analyses is to fix the system damping. Two damping mechanisms are modelled. The first is material damping in the elastic bodies which is presumed to be proportional damping of the form

$$\mathbf{C} = \mu\mathbf{M} + \eta\mathbf{K}, \tag{21}$$

where **M**, **K** are the inertia and stiffness matrices and μ, η are constant Rayleigh coefficients. This represents the primary energy dissipation in the model. The coefficients μ, η are adjusted such that the logarithmic decrement [13] of the impact analysis DTE yields a 7% damping ratio. The second damping is linear, viscous damping acting at the gear rotation axis (i.e., viscous bearing damping). The bearing damping is light, and the chosen value ($<1\%$) was the minimum required to remove numerically induced "drift" in the mean-transmission error due to response in the rigid-body mode.

The primary intent of this work is to examine the dynamic response under operating speeds and torques. The complex DTE response that occurs in this simplest of gear sets is shown in Figure 4 for $T = 150$ N m from reference [4]. A primary resonance is evident for mesh frequency $f_m \approx f_n \approx 2700$ Hz. A distinct softening non-linearity exists as the peak bends to the left. In a speed range just below 2500 Hz, multiple steady state response amplitudes are possible. Classical jump phenomena occur as the speed increases or decreases past the boundaries of the multiple solution regime. Blankenship and Kahraman [4] report 10–40 dB differences in sound pressure level between these branches. The resonances at speeds one-half and one-third of the primary resonance speed are caused by higher harmonics of mesh frequency in the dynamic excitation. The dynamic mesh forces have spectral content at (at least) the harmonics of mesh frequency, that is,

$$F_{mesh}(t) = \sum D_p \sin(2\pi p f_m t + \phi_p) + g(t). \tag{22}$$

At $f_m = f_n/2 = 1350$ Hz, the second harmonic of mesh frequency ($p = 2$) coincides with f_n, exciting resonance. The third harmonic of mesh frequency ($p = 3$) drives the resonance at

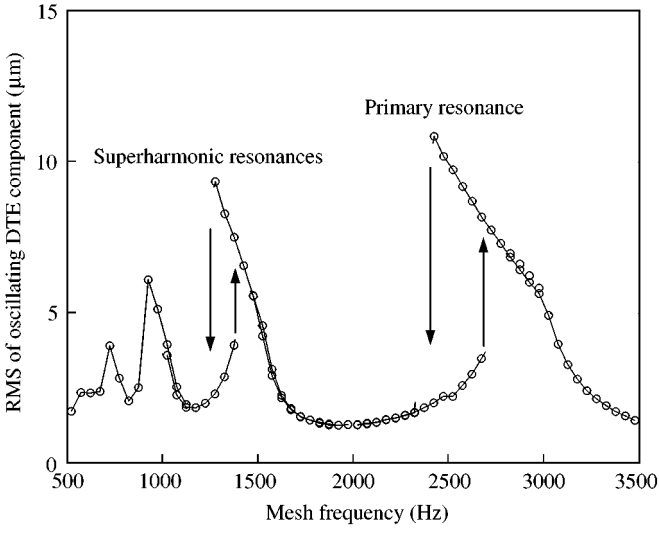

Figure 5. Finite element calculation of RMS of oscillating component of dynamic transmission error for $T = 150$ N m.

$f_m = f_n/3$. The softening non-linearity and jump phenomena are less pronounced in these superharmonic resonances.

Figure 5 shows the corresponding finite element DTE results. The multiple resonances, softening non-linearity, and jump phenomena are predicted remarkably well by the finite element analysis. The frequencies at which the resonances and jumps occur is slightly higher for the finite element results because of the aforementioned natural frequency differences. Notice that even the quantitative amplitudes of the finite element model agree quite well with the experimental data.

Figure 6 from reference [4] presents the experimental DTE amplitudes for three torques $T = 100$, 200, and 300 N m. Responses were measured for slowly increasing and decreasing speeds to calculate the lower and upper branches respectively. The multiple resonances and non-linear jumps exhibited in Figure 4 persist for both higher and lower torques. The amplitude of resonant response is noticeably larger for increasing torque. Analogous FE/CM results in Figure 7 agree closely with experimental data. In particular, the jump frequencies and maximum amplitudes generally agree *quantitatively* as well as qualitatively. One exception is the width of the multiple solution band for $T = 100$ N m, where the computational results predict a wider overlap.

Unlike typical analyses, there is no freedom to adjust the excitation or system parameters to achieve this agreement. The results are particularly encouraging in light of this point. The only unspecified parameter is damping, which was fixed at 7% as discussed previously. This value was selected so that the jump down frequency for the $T = 100$ N m case agreed with experimental measurements. Once selected, the value was fixed and good agreement resulted for other torques.

Figure 8 shows the time-domain DTE and the spectra for the primary resonance case of $T = 150$ N m (Figures 4 and 5). The DTE for the upper branch (Figures 8(a) and 8(c) is nearly harmonic at the mesh frequency. Some small distortion from higher harmonics is evident in the primary resonance lower branch (Figures 8(b) and 8(d)). Figure 9 presents analogous data for the resonance condition at $f_m = 1350$ Hz. In this case, the response is almost harmonic at twice the mesh frequency, that is, the natural frequency. The upper

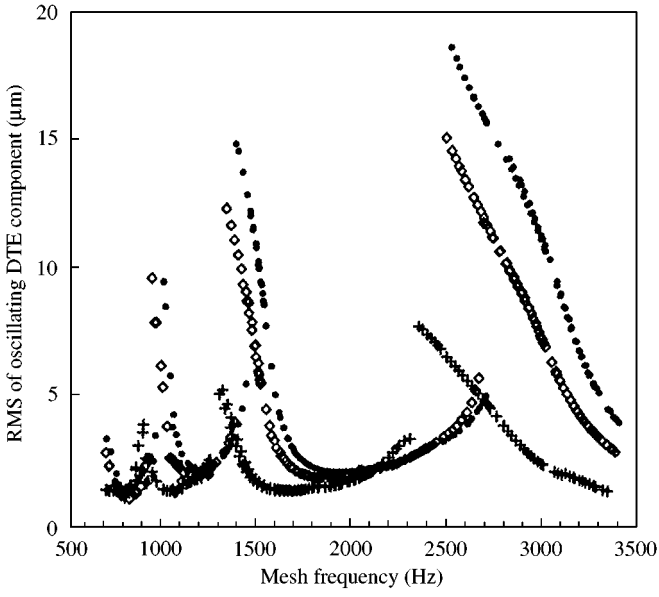

Figure 6. Experimentally measured RMS of oscillating component of dynamic transmission error for $T = 100$ (+), 200 (◇) and 300 (∗) N m. From reference [4].

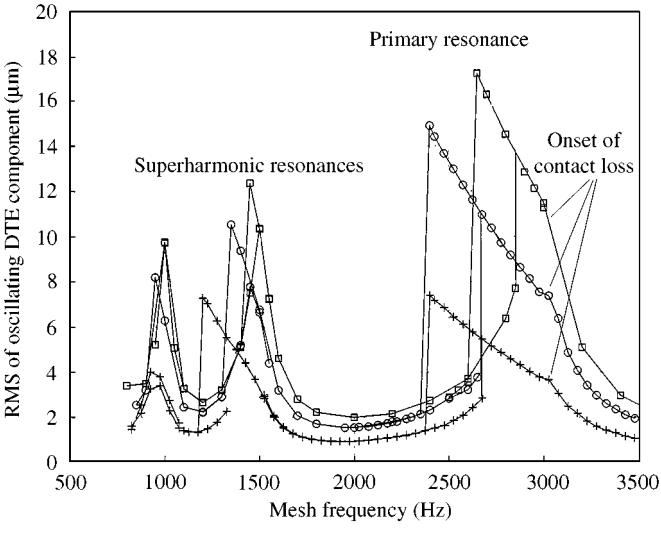

Figure 7. Finite element calculation of RMS of oscillating component of dynamic transmission error for $T = 100$ (+), 200 (○) and 300 (□) N m.

branch, which has considerably higher amplitude, is closer to purely harmonic response while the lower branch has more distortion from frequencies other than the resonant excitation frequency at the second harmonic of f_m. These time-domain calculations closely match the experimental data [4].

The softening non-linearity exhibited in the frequency response indicates a stiffness reduction. The reduced stiffness is caused by contact loss at the tooth mesh. Figure 10 shows

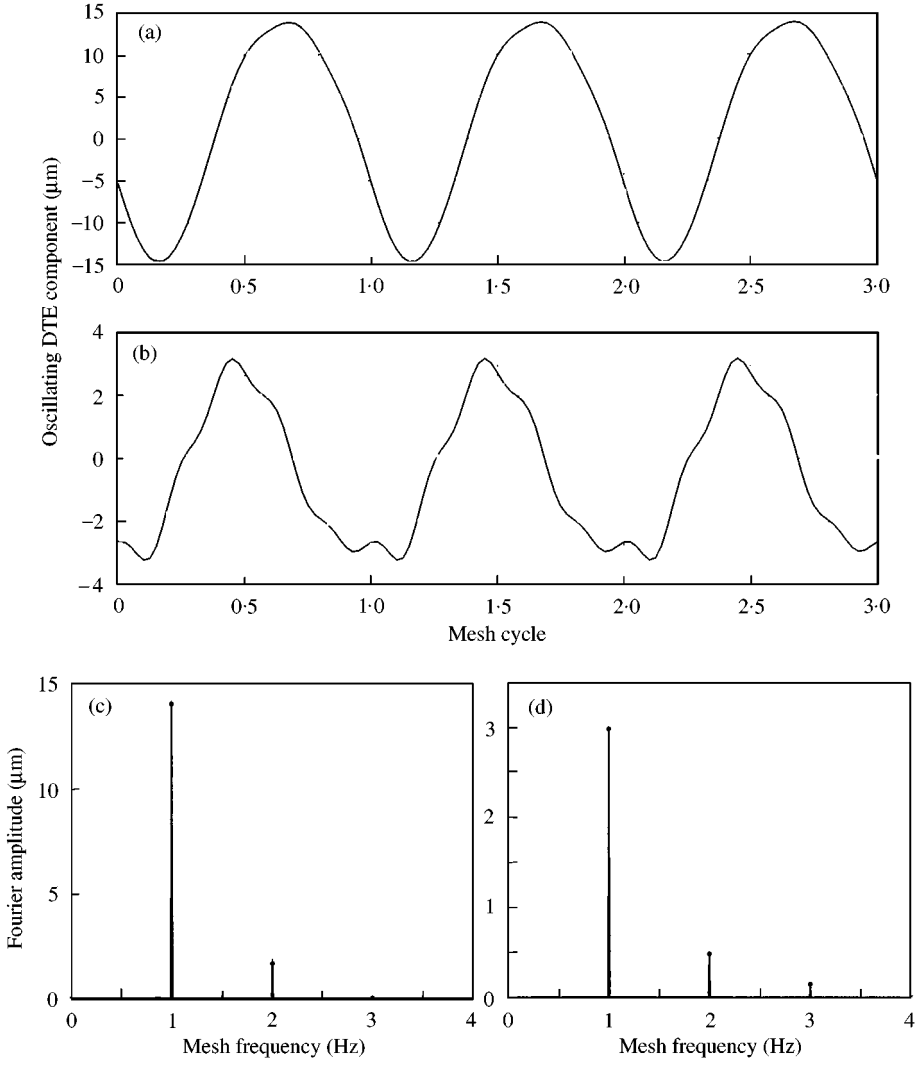

Figure 8. Oscillating DTE time histories and spectra for the (a, c) upper and (b, d) lower branches of the primary resonance for $f_m = 2400$ Hz and $T = 150$ N m.

the net tooth mesh force for the upper and lower branches of the primary resonance of Figure 5 ($T = 150$ N m, $f_m = 2500$ Hz). The mesh force (or tooth load) in Figure 10(a) for the lower branch of primary resonance exhibits a smooth load carrying transition between a tooth i and its adjacent tooth $i + 1$. No contact loss occurs. For operation at the same speed along the upper branch (Figure 10(b)), however, the mesh force vanishes over part of each mesh cycle. Contact loss is clearly the non-linearity source. Tooth loads for the upper and lower branches of the secondary resonance at $f_m = 1350$ Hz are given in Figure 11. While the lower branch (Figure 11(a)) has no contact loss, the upper branch (Figure 11(b)) has two contact losses in each mesh cycle, consistent with the dominant response frequency being twice the mesh frequency. The maximum tooth load is considerably larger when contact loss occurs. Comparing Figures 10(a) and 10(b) for primary resonance, the maximum tooth load with contact loss (upper branch) is 4850 N, a 62% increase from the maximum load of 3000 N for the same speed without contact loss (lower branch). In conflict

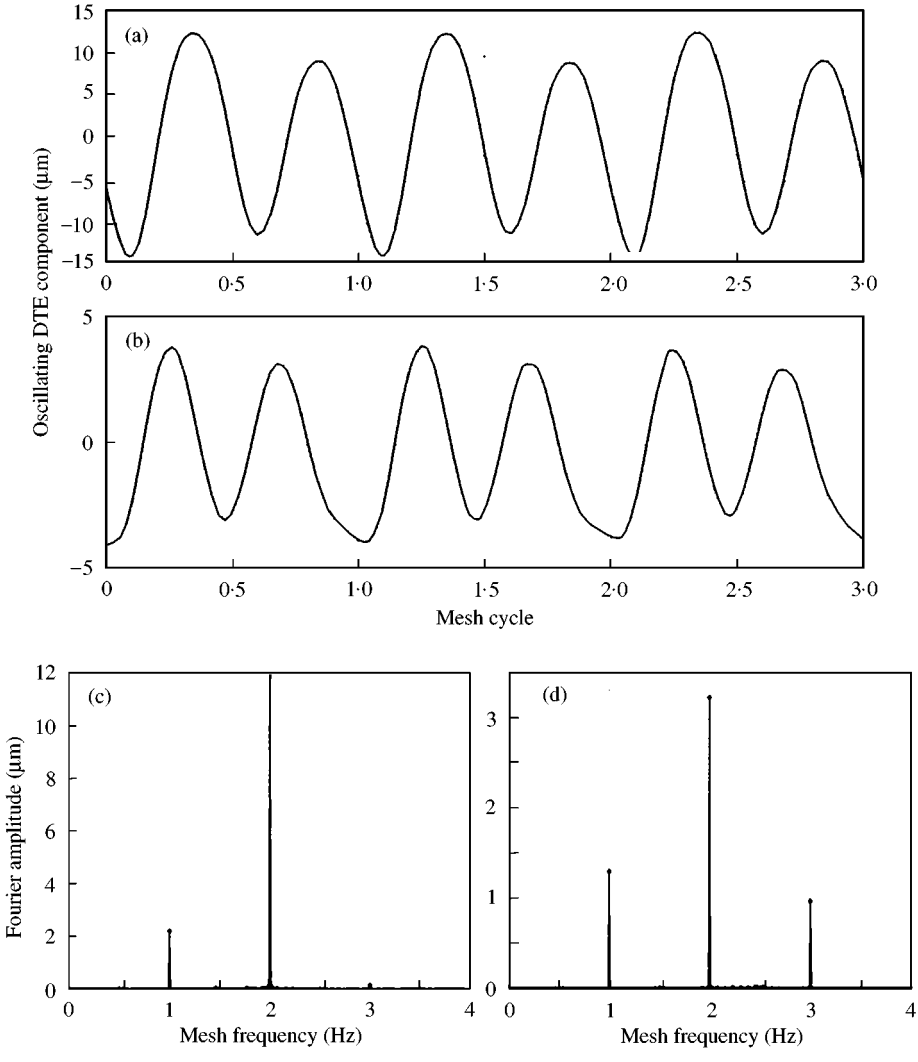

Figure 9. Oscillating DTE time histories and spectra for the (a, c) upper and (b, d) lower branches of the secondary resonance for $f_m = 1300$ Hz and $T = 150$ N m.

with conventional assumptions about gear behavior, contact loss occurs even for large torques as in the $T = 300$ N m case of Figure 7. As a numerical experiment, a speed sweep analogous to Figure 5 and 7 was conducted for a torque of 600 N m. The character of the response is the same as for the presented torques in that contact loss and the associated jump phenomena occur despite the large torque and the maximum amplitude was considerably greater than for $T = 300$ N m. Non-linear behavior is apparently unavoidable in this gear system.

Contact loss is not limited to mesh frequencies in the immediate vicinity of the jump down phenomenon. In fact, it is not limited to the regime in which multiple steady state solutions exist. Considering Figure 7, a kink in the frequency response curve occurs just above the natural frequency for each torque value. This kink indicates the onset of contact loss, which occurs for all mesh frequencies along the upper branch between the kink and the jump down. Contact loss never occurs along the lower branch.

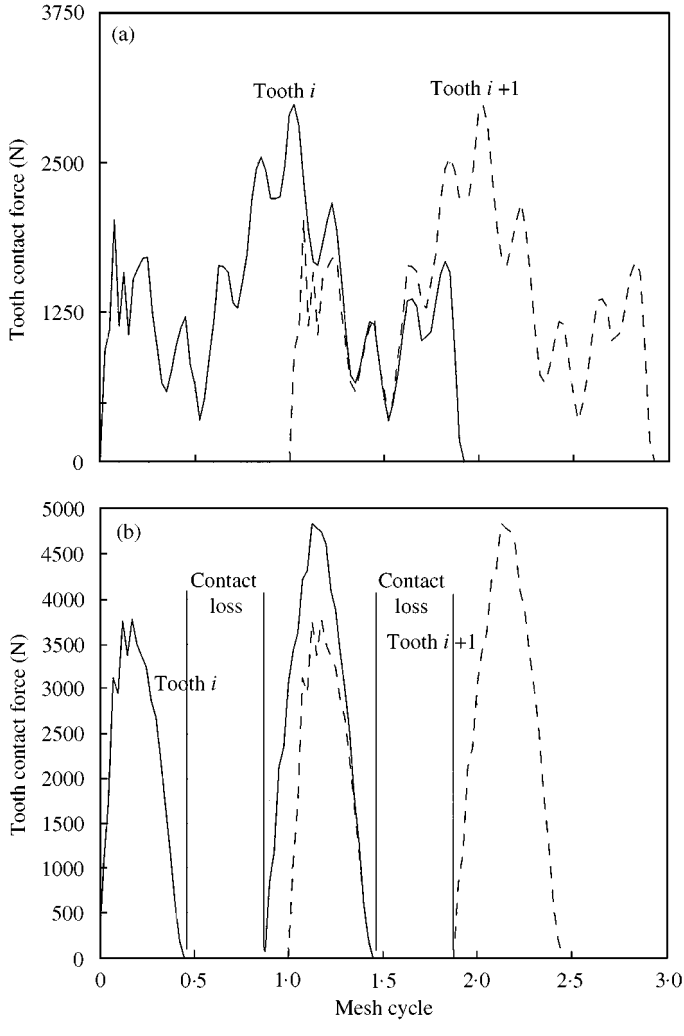

Figure 10. Tooth loads for contacting teeth at the (a) upper and (b) lower branches of the primary resonance for $f_m = 2400$ Hz and $T = 150$ N m.

3. SINGLE-DEGREE-OF FREEDOM ANALYSIS

Analytical representations of the gear response in terms of dynamic systems having few degrees of freedom is desirable from research and design perspectives, and many have been proposed [1]. The following results show that such models are capable of producing good results but are limited by their high sensitivity to mesh force modelling. Two models are examined, with the difference in each being the representation of the varying mesh stiffness as the gears rotate. The basic model is based on Figure 2 with the equation of motion.

$$m\ddot{x} + c\dot{x} + F(t) = T/r, \quad F(t) = \begin{cases} k(t)x, & x \geqslant 0, \\ 0, & x < 0. \end{cases} \tag{23}$$

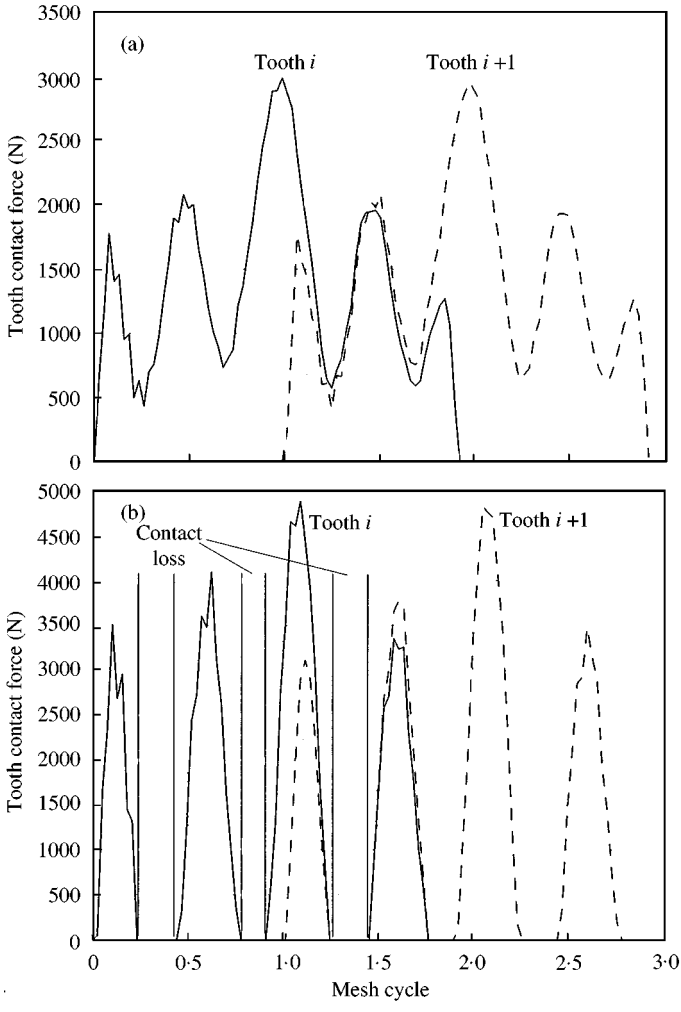

Figure 11. Tooth loads for contacting teeth at the (a) upper and (b) lower branches of the secondary resonance for $f_m = 1300$ Hz and $T = 150$ N m.

Here, $x = r_2\theta_2 + r_1\theta_1$ is the DTE, $m = I_1I_2/(I_1r_1^2 + I_2r_2^2) = I/(2r^2)$, $F(t)$ is the elastic mesh force, and T is a steady torque. The configuration $x = 0$ implies the condition where a pair of teeth are in unloaded contact. Blankenship and Kahraman [8] studied a similar model using harmonic balance to gain analytical insight into the non-linear response of spur gears. The damping c is chosen to give a damping ratio of 8%. Note that this damping represents dissipation by a discrete viscous damper at the tooth mesh rather than material damping distributed throughout the gears as in the finite element model, and this is why the damping ratios differ slightly. $m = 1{\cdot}4$ kg is chosen such that $f_n = (1/2\pi)\sqrt{k_{avg}/m} = 2900$ Hz in accordance with the finite element model and the average mesh stiffness $k_{avg} = 462{\cdot}1 \times 10^6$ N/m is determined from results to follow. The mesh stiffness is both non-linear and time varying. Equation (23) is numerically integrated with the stiffness $k(t)$ at each instant determined from Figure 13 using the nominal position of the gears in the mesh cycle.

Certain static results are needed before proceeding. First, the static transmission error and its spectrum are calculated over a mesh cycle for the torques $T = 100$, 200, and 300 N m

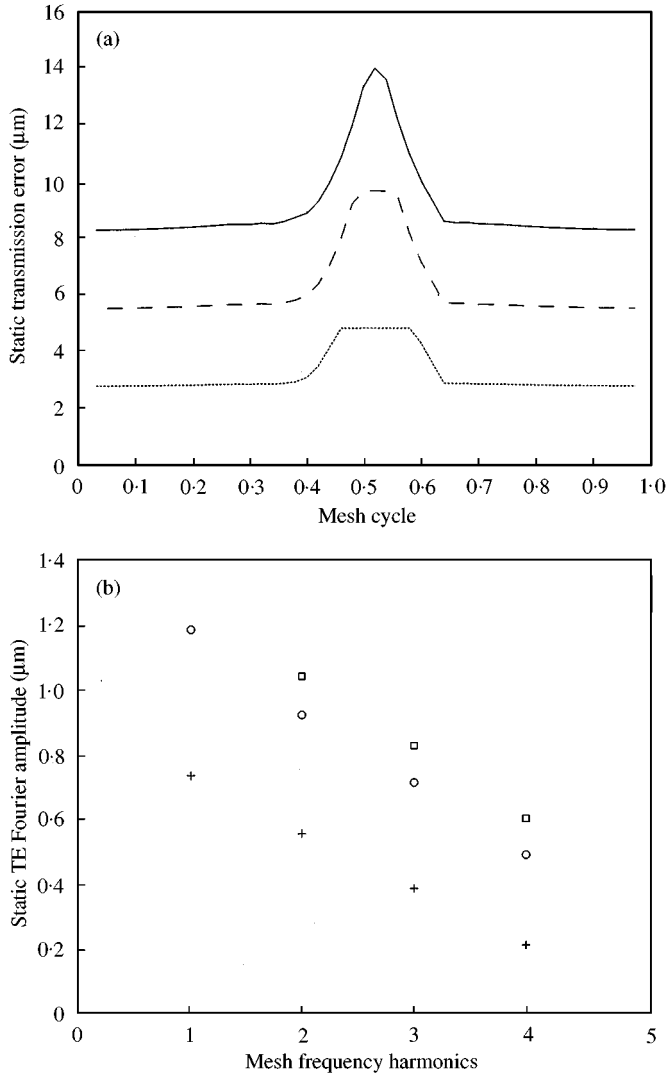

Figure 12. Static transmission error for $T = 100$ N m (····), 200 N m (- - -), and 300 N m (——). (b) Static transmission error spectrum for $T = 100$ N m (+), 200 N m (○), and 300 N m (□).

from static finite element analyses (Figure 12). Some models use static transmission error to represent the input excitation in s.d.o.f. dynamic models. Using the relationship $k = (T/r)/STE$ for a base radius of 7·047 mm, the mesh stiffness is determined along with its spectral content (Figure 13). The weighted line is the rectangular wave approximation where the abrupt changes coincide with the changes in the number of tooth pairs in contact.

The first mesh stiffness model uses the torque-independent rectangular waveform in Figure 13. Figure 14 shows the DTE determined for both increasing and decreasing speed sweeps. The oscillating component of DTE (Figure 14(a)) reproduces the experimental amplitudes, jump phenomena, and superharmonic resonances with reasonable accuracy. A distinct difference, however, is that the jump frequencies, like the stiffness model, are independent of torque. The mean DTE (Figure 14(b)) experiences jumps coinciding with

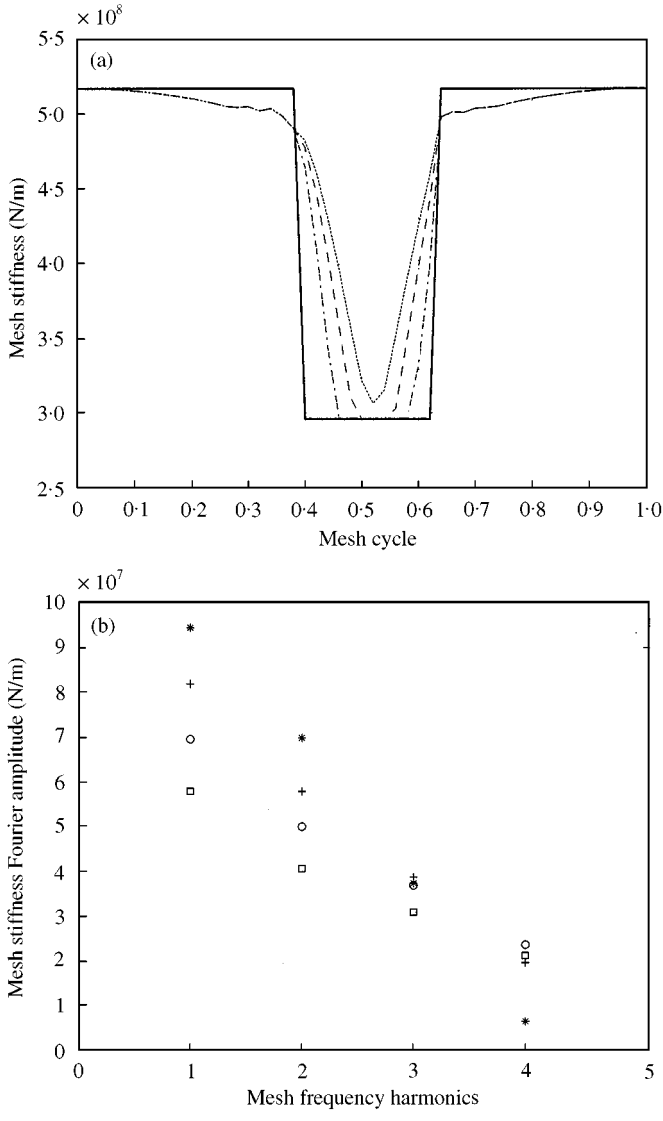

Figure 13. (a) Mesh stiffness (derived from static transmission error) for rectangular wave approximation (——), $T = 100$ N m (– · –), 200 N m (- - -), and 300 N m (· · · ·). (b) Mesh stiffness spectrum for rectangular wave approximation (*), $T = 100$ N m (+), 200 N m (○), and 300 N m (□).

those in the oscillating DTE. As the amplitude of oscillating DTE jumps down (or up), the mean DTE jumps up (or down). The changes in mean DTE, however, are consistently less than the corresponding oscillating DTE changes.

The mesh forces $F(t)$ from this s.d.o.f. model are shown in Figure 15 for the upper and lower branches of the primary resonance for $T = 150$ N m. Contact loss is evident along the upper branch. Again, this contact loss starts at the kinks in the frequency response curves around $f_m = 3100$ Hz. No contact loss occurs in the lower branch. Note that Figure 15 gives the total mesh force and must be compared with the sum of the two tooth loads in Figure 10. Figure 15 exposes a shortcoming of this s.d.o.f model. Notice the discontinuity in the mesh force $F(t) = k(t)x(t)$ that occurs as the number of teeth in contact changes. This occurs

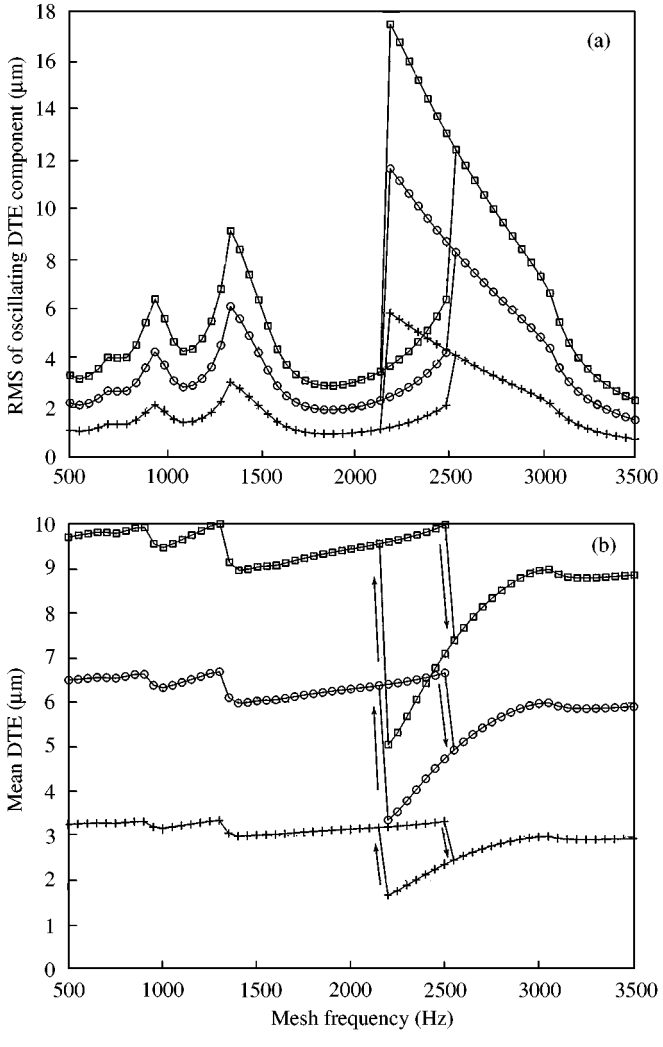

Figure 14. Single-degree-of-freedom model RMS of oscillating DTE component and mean DTE for $T = 100$ N m (+), 200 N m (○), and 300 N m (□). Mesh stiffness is the rectangular waveform in Figure 13.

because $k(t)$ undergoes a step change while $x(t)$ cannot change instantly. In reality, the tooth entering contact will more gradually absorb the mesh force.

In an effort to improve the s.d.o.f. model to better match the torque sensitivity of the jump frequencies, a second mesh stiffness model was introduced. In this case, the instantaneous mesh stiffness is determined from Figure 13 using the curve for the appropriate torque. The dynamic response results are shown in Figure 16. While this stiffness model appears more representative of the physical system and differs relatively modestly from the rectangular waveform stiffness, the results are markedly different and do not agree with the experiment. The oscillating DTE amplitudes are strikingly reduced. Furthermore, contact loss occurs only at low torques with linear behavior for $T = 200$ and 300 N m. The results indicate that the shape of the assumed mesh stiffness function is critical. While the average mesh stiffness changes little with torque (Figure 13(a)), the altered shape sharply changes the Fourier spectrum with torque (Figure 13(b)). Accurate Fourier representation of the

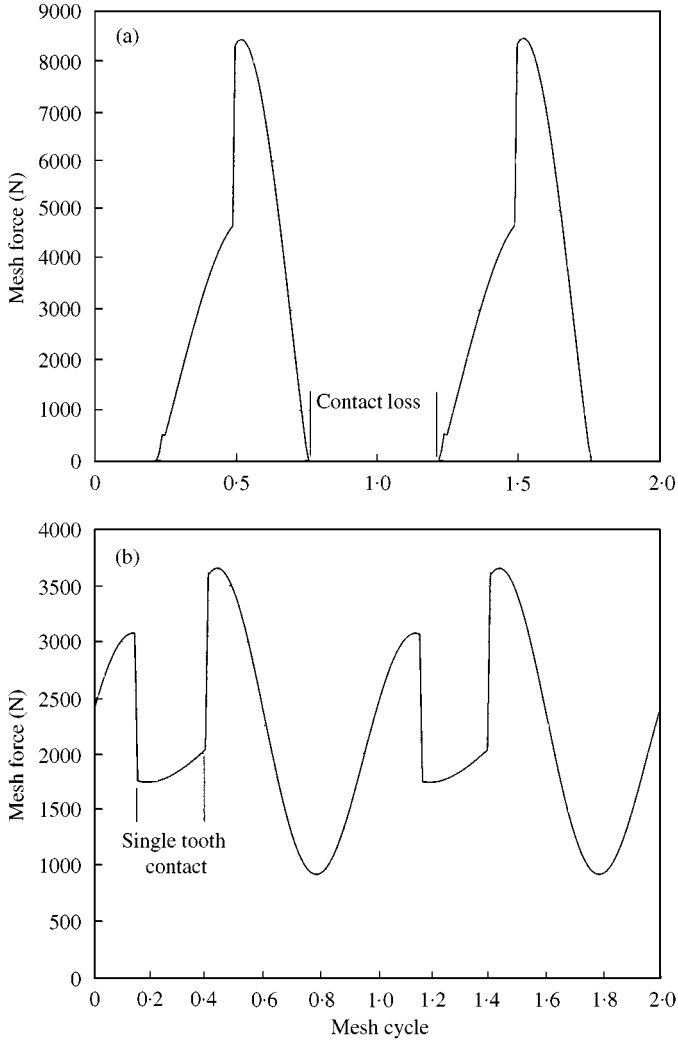

Figure 15. Net mesh force for the single-degree-of-freedom model with rectangular waveform mesh stiffness approximation. Curves are shown for the (a) upper branch ($f_m = 2200$ Hz) and (b) lower branch ($f_m = 2150$ Hz) of the primary resonance with $T = 150$ N m.

changing stiffness is evidently crucial in the use of low order dynamic models such as equation (23).

4. DISCUSSION AND SUMMARY

This paper presents a finite element/contact mechanics formulation that is well suited to dynamic gear analyses. The critically important mesh forces are determined by contact analysis in combination with a unique semi-analytical finite element formulation at the tooth mesh. No assumptions are made with regard to modelling one or both of mesh stiffness variation and static transmission error as approximations of the dynamic excitation [12]. This combination overcomes the usual limitation of finite element analysis

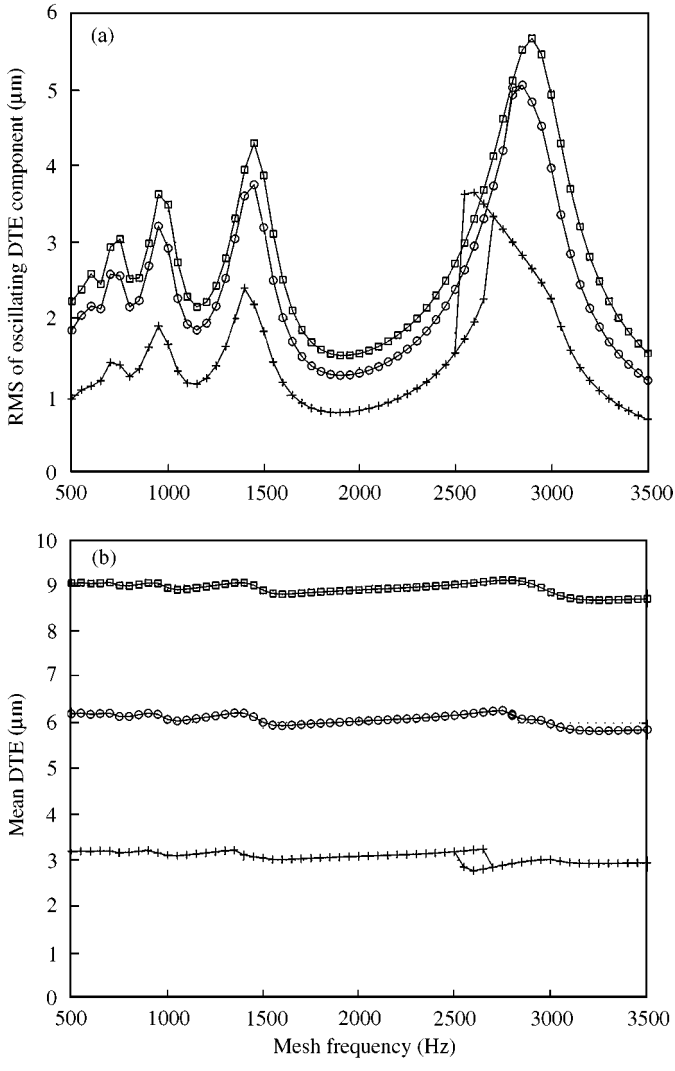

Figure 16. Single-degree-of-freedom model RMS of oscillating DTE component and mean DTE for $T = 100$ N m (+), 200 N m (○), and 300 N m (□). Mesh stiffnesses for each torque value are shown in Figure 13.

to static analyses, free vibration eigensolutions, or response calculations with inherent assumptions on the nature of the mesh forces. The excellent agreement with experimental data demonstrates the ability to capture complex, non-linear phenomena. The approach is particularly valuable for multi-body, multi-mesh systems such as epicyclic gears where mesh modelling in discrete dynamic models is especially difficult. Additional features that result from the finite element approach are that coupling to flexible shafts, bearings, and housings can be handled naturally, gear geometry errors and tooth-to-tooth variability can be easily analyzed, elastic deformations of the gear bodies are modelled, friction at the tooth surface can be included in the contact analysis [10], and profile modifications of magnitudes used in practice are modelled by the redefinition of the tooth surface without remeshing. This last point is true because local tooth deformations near the surface are handled by an analytical model near the inner region of Figure 3; *small* profile modifications affect $\mathbf{A}_{local}$ in equation (17) and not the finite element matrices in equation (6).

A discrete, s.d.o.f. model with contact loss non-linearity and time-varying mesh stiffness captures much of the non-linear behavior. Two differing stiffness models yield perplexingly different results. When the stiffness is a torque-independent, rectangular wave function of mesh cycle (one of the simplest approximations) much of the non-linear behavior is accurately predicted. Counter-intuitively, when the expectedly more accurate torque-dependent stiffness curves (Figure 13) are used, the non-linear behavior is suppressed at high torques, which clearly conflicts with the experiments. The spectral content of the rectangular wave in the lower mesh frequency harmonics is lost in the torque-specific stiffness approximations, and this difference appears to be the cause of the large difference in results. It is troublesome that the expectedly better model produces poorer agreement with experiments. While the results show that low order models are able to capture complex, dynamic response in this case, the high sensitivity to stiffness modelling makes use of such models for other gear systems uncertain without further validation.

ACKNOWLEDGMENTS

The authors thank T. L. Krantz of the Army Research Lab for helpful discussions and advice throughout the work. This material is based on work supported by the NASA Glenn Research Center under Grant NAG3-1979 and the US Army Research Office under Grant DAAD19-99-1-0218.

REFERENCES

1. H. N. Ozguven and D. R. Houser 1988 *Journal of Sound and Vibration* **121**, 383–411. Mathematical-models used in gear dynamics—A review.
2. P. Velex and M. Maatar 1996 *Journal of Sound and Vibration* **191**, 629–660. A mathematical-model for analyzing the influence of shape deviations and mounting errors on gear dynamic behavior.
3. G. W. Blankenship and R. Singh 1992 *ASME 6th Power Transmission and Gearing Conference Phoenix*. DE-43-1, 137–146. A comparative study of selected gear mesh force interface dynamic models.
4. G. W. Blankenship and A. Kahraman 1996 *ASME Power Transmission and Gearing Conference, San Diego*. Gear dynamics experiments, Part-I: characterization of forced response.
5. A. Kahraman and G. W. Blankenship 1996 *ASME Power Transmission and Gearing Conference, San Diego*. Gear dynamics experiments, Part-II: effect of involute contact ratio.
6. A. Kahraman and G. W. Blankenship 1996 *ASME Power Transmission and Gearing Conference, San Diego*. Gear dynamics experiments, Part-III: effect of involute tip relief.
7. A. Kahraman and G. W. Blankenship 1997 *Journal of Applied Mechanics* **64**, 217–226. Experiments on nonlinear dynamic behavior of an oscillator with clearance and periodically time-varying parameters.
8. G. W. Blankenship and A. Kahraman 1995 *Journal of Sound and Vibration* **185**, 743–765. Steady state forced response of a mechanical oscillator with combined parametric excitation and clearance type non-linearity.
9. R. G. Parker, V. Agashe and S. M. Vijayakar 2000 *ASME Journal of Mechanical Design* **122**, 305–311. Dynamic response of a planetary gear system using a finite element/contact mechanics model.
10. S. Vijayakar, H. Busby and D. Houser 1988 *Computers and Structures* **29**, 569–576. Linearization of multibody frictional contact problems.
11. S. M. Vijayakar 1991 *International Journal for Numerical Methods in Engineering* **31**, 524–546. A combined surface integral and finite element solution for a three-dimensional contact problem.
12. H. N. Ozguven and D. R. Houser 1988 *Journal of Sound and Vibration* **125**, 71–83. Dynamic analysis of high-speed gears by using loaded static transmission error.
13. D. J. Inman 1996 *Engineering Vibration*. Englewood Cliffs, NJ: Prentice-Hall.